



# Imparting selective polysulfide conversion via geminal-atom moieties in lithium-sulfur batteries

Yifan Ding<sup>a,1</sup>, Tianran Yan<sup>b,1</sup>, Jianghua Wu<sup>c,1</sup>, Meng Tian<sup>d,\*</sup>, Miaoyu Lu<sup>a</sup>, Conglei Xu<sup>e</sup>,  
Jiayi Gu<sup>a</sup>, Haorui Zhao<sup>a</sup>, Yifei Wang<sup>e,\*</sup>, Xiaoqing Pan<sup>c</sup>, Shi Xue Dou<sup>f</sup>, Liang Zhang<sup>b,\*</sup>,  
Jingyu Sun<sup>a,\*</sup>

<sup>a</sup> College of Energy, Soochow Institute for Energy and Materials Innovations, Jiangsu Provincial Key Laboratory for Advanced Carbon Materials and Wearable Energy Technologies, Soochow University, Suzhou 215006, China

<sup>b</sup> Institute of Functional Nano & Soft Materials, Jiangsu Provincial Key Laboratory for Carbon-Based Functional Materials and Devices, Soochow University, Suzhou 215006, China

<sup>c</sup> i-Lab, CAS Center for Excellence in Nanoscience, Suzhou Institute of Nano-Tech and Nano-Bionics, Chinese Academy of Sciences, Suzhou 215123, China

<sup>d</sup> Interdisciplinary Center for Fundamental and Frontier Sciences, Nanjing University of Science and Technology, Jiangyin 214443, China

<sup>e</sup> National Engineering Laboratory for Advanced Municipal Wastewater Treatment and Reuse Technology, Key Laboratory of Beijing for Water Quality Science and Water Environment Recovery Engineering, Beijing University of Technology, Beijing 100124, China

<sup>f</sup> Institute of Energy Materials Science, University of Shanghai for Science and Technology, Shanghai 200093, China

## ARTICLE INFO

### Keywords:

Li-S chemistry  
Selective catalysis  
Geminal-atom mediator  
Reaction kinetics  
Bidirectional

## ABSTRACT

Electrocatalysis in lithium-sulfur (Li-S) chemistry has readily stimulated extensive interests because of its irreplaceable role in realizing high-performance batteries. In this sense, achieving accelerated catalytic conversion of polysulfides is essential for the shuttle inhibition and kinetics promotion. Nonetheless, selective catalysis of sulfur reduction/evolution reaction via precise control over electrocatalytic mediators is still in its infancy. Moreover, specific catalytic role of the active metal center in dual-atom catalyst sites remains relatively unexplored. Herein, we utilize a salt-confined strategy to fabricate FeCo geminal-atom moieties dispersed on N-doped carbon support (FeCo-NC) for Li-S batteries throughout leveraging Fe and Co single-atom species with selective catalysis. The enhanced bidirectional conversion kinetics of polysulfide with the incorporation of Fe and Co atoms are uncovered throughout theoretical simulation and electrokinetic analysis. As a result, the FeCo-NC endows a rechargeable Li-S battery with excellent capacity retention rate of 98.6% after 100 cycles at 0.2 C and cycling stability with a decay rate of 0.033% per cycle over 2000 cycles at 3.0 C. More encouragingly, the assembled Li-S cell at a sulfur loading of 6.7 mg cm<sup>-2</sup> can harvest an areal capacity of 7.13 mAh cm<sup>-2</sup>, signifying the rational design of geminal-atom mediators to dictate selective catalysis behaviors toward practical Li-S batteries.

## 1. Introduction

Lithium-sulfur (Li-S) battery has attracted tremendous attention in energy storage realms owing to its high theoretical capacity (1675 mAh g<sup>-1</sup>) and energy density (2600 Wh kg<sup>-1</sup>) [1–6]. Nevertheless, the notorious lithium polysulfide (LiPS) shuttling and the sluggish reaction kinetics seriously jeopardize the electrochemical performance, inevitably giving rise to inferior sulfur utilization and short cyclic lifespan [7–10]. In particular, the conversion kinetics of LiPSs plays a key role in determining the electrochemical performance of Li-S batteries, which are

closely related to other issues exacerbating polysulfide shuttling and reducing battery cyclability. Therefore, achieving accelerated catalytic conversion of LiPSs is essential for the inhibition of shuttle effect as well as the promotion of electrochemical kinetics [11–13]. Previous studies employed various mediators to boost the LiPS conversion in sulfur cathodes and achieved satisfactory results toward high-performance Li-S batteries [14–17]. Although the intrinsic link between catalyst moieties and catalytic pathways has not been well addressed, these studies indeed suggest the positive impacts by the use of electrocatalysts.

The charge-discharge process in the commonly recognized Li-S

\* Corresponding authors.

E-mail addresses: [tianmeng@njust.edu.cn](mailto:tianmeng@njust.edu.cn) (M. Tian), [wangyifei@bjut.edu.cn](mailto:wangyifei@bjut.edu.cn) (Y. Wang), [liangzhang2019@suda.edu.cn](mailto:liangzhang2019@suda.edu.cn) (L. Zhang), [sunjy86@suda.edu.cn](mailto:sunjy86@suda.edu.cn) (J. Sun).

<sup>1</sup> Y.F.D., T.R.Y. and J.H.W. contributed equally.

system corresponds to the redox process of the active sulfur species in the cathode. Fundamentally, it is necessary to consider the two reversible chemical processes of sulfur reduction reaction (SRR) and sulfur evolution reaction (SER) for boosted sulfur electrochemistry [18–20]. Therefore, it is equally important for both processes to garner rapid polysulfide catalytic conversion. Latest research endeavors have witnessed fine management of polysulfides via electrocatalysts with dual-directional catalytic effects over SRR and SER processes [21,22]. The selective catalysis has become a surge of interest in catalysis such as  $\text{CO}_2$ ,  $\text{N}_2$ , and  $\text{O}_2$  reduction reactions [23–25]. However, selective catalysis of SRR and SER with different reaction paths in Li–S chemistry is still in its infancy [26].

To obtain ideal bifunctional catalysts, the electrocatalyst screening of SRR and SER active components is an important step. Single-atom catalysts (SACs) have stimulated extensive attention in recent years and gradually become an active research frontier because of the optimal atom utilization efficiency and highly exposed active sites [27–31]. Limited by the single electronic structure and sole active center of SACs, double-atom catalysts (DACs) have been accordingly developed [32,33]. In the field of Li–S chemistry, recent studies revealed that DACs harness a favorable catalytic effect on sulfur redox, especially the reported mediators comprising Fe and Co metal atoms [34–36]. Nevertheless, it remains a grand challenge to precisely control geminal-atomic sites within carbon matrix with different selectivity for the SRR and SER. In addition, the specific catalytic role of the active metal center for sulfur redox in DACs needs to be further explored. Therefore, the target design of Fe–Co DAC is a promising strategy to endow single-atomic Fe and Co sites with excellent bifunctional property.

Herein, we utilize a salt-confined strategy to fabricate FeCo geminal-atom species dispersed on N-doped carbon framework (FeCo-NC), harnessing a metal loading of 3.5 wt%. Such a salt templating route mitigates the collapse of carbonaceous support during pyrolysis, thereby leading to the considerable elevation of metal loading capacity and large specific surface area for high-quality sulfur host. Theoretical calculations reveal that the SRR activity follows the order of  $\text{Fe} > \text{Co}$ , whereas the SER activity obey  $\text{Co} > \text{Fe}$  in sulfur redox process. Guided by this result, Fe and Co geminal-atom with selective catalytic ability is coupled to achieve efficient bidirectional catalytic conversion of LiPSs. Exhaustive electrochemical characterization and operando instrumental probing further substantiate the boosted bidirectional polysulfide conversion via FeCo-NC electrocatalyst, implying the selective catalysis effects in Li–S chemistry. As a result, the S/FeCo-NC cathode obtains impressive electrochemical performances with a specific capacity of 1303.9  $\text{mAh g}^{-1}$  at 0.2 C and 775.9  $\text{mAh g}^{-1}$  at 3.0 C, respectively. It can also harvest a high capacity retention of 98.6% at 0.2 C after 100 cycles and a low capacity decay of 0.033% per cycle after 2000 cycles at 3.0 C. Assembled cells with a sulfur loading of 6.7  $\text{mg cm}^{-2}$  can also achieve an areal capacity of 7.13  $\text{mAh cm}^{-2}$ .

## 2. Experimental section

### 2.1. Synthesis of Zn-ZIF

4 g  $\text{Zn}(\text{NO}_3)_2 \cdot 6 \text{H}_2\text{O}$  was dissolved in 100 mL methanol to form homogeneous solution. Next, 4 g 2-methylimidazole (2-MIM) in 100 mL methanol was added in the above-mentioned solution. The mixture was stirred at room temperature for 24 h. The as-obtained samples were centrifuged, washed with deionized water and ethanol for several times and further dried at 80 °C for overnight and named as Zn-ZIF.

### 2.2. Synthesis of ZnCo-ZIF

4 g  $\text{Zn}(\text{NO}_3)_2 \cdot 6 \text{H}_2\text{O}$  and 0.1 g  $\text{Co}(\text{NO}_3)_2 \cdot 6 \text{H}_2\text{O}$  (Zn: Co=40: 1) were dissolved in 100 mL methanol to form homogeneous solution. Next, 4 g 2-methylimidazole (2-MIM) in 100 mL methanol was added in the above-mentioned solution. The mixture was stirred at room temperature

for 24 h. The as-obtained samples were centrifuged, washed with deionized water and ethanol for several times and further dried at 80 °C for overnight and named as ZnCo-ZIF.

### 2.3. Synthesis of $\text{NaCl}@\text{Zn-ZIF}$ and $\text{NaCl}@\text{ZnCo-ZIF}$

Thus-produced Zn-ZIF and ZnCo-ZIF crystals were evenly distributed in a saturated NaCl salt solution (8 g NaCl dissolved in 20 mL deionized water) by ultrasonication under stirring. Upon continuously adding ethanol, a NaCl recrystallization process occurred in such a mixed solution. Finally,  $\text{NaCl}@\text{Zn-ZIF}$  and  $\text{NaCl}@\text{ZnCo-ZIF}$  were obtained by filtration and drying in an oven at 60 °C for 12 h.

### 2.4. Synthesis of NC

The powder of  $\text{NaCl}@\text{Zn-ZIF}$  was placed in a tube furnace and heated to 900 °C at 5 °C  $\text{min}^{-1}$ , held at 900 °C for 2 h in flowing Ar and cooled down to room temperature. NaCl was removed with deionized water and then dried to obtain the NC.

### 2.5. Synthesis of Co-NC

The  $\text{NaCl}@\text{ZnCo-ZIF}$  was heated at 900 °C for 2 h with a heating rate of 5 °C  $\text{min}^{-1}$  under the Ar atmosphere. The obtained powder was added to the 0.5 M  $\text{H}_2\text{SO}_4$  solution, which was stirred at 60 °C for 12 h to remove the NaCl and Co metal clusters. Finally, the Co-NC was obtained by centrifugation and washed three times with deionized water.

### 2.6. Synthesis of Fe-NC

100 mg NC was added equably in 20 mL deionized water with ultrasonication. Then 0.5 M  $\text{FeSO}_4$  and 0.15 M 1,10-phenanthroline (1:3) were added to the dispersion solution while ultrasonic and stirred at room temperature for 12 h. The filtered and dried powder was annealed at 700 °C under Ar for 1 h to obtain the Fe-NC.

### 2.7. Synthesis of FeCo-NC

100 mg Co-NC was added equably in 20 mL deionized water with ultrasonication. 0.5 M  $\text{FeSO}_4$  and 0.15 M 1,10-phenanthroline (1:3) were added to the Co-NC solution while ultrasonic and stirred at room temperature for 12 h. Then the resulting mixture is dried after strained at 60 °C for 12 h. Finally, the FeCo-NC was obtained by annealed at 700 °C under Ar for 1 h to obtain the FeCo-NC.

### 2.8. Synthesis of S/FeCo-NC, S/Co-NC and S/Fe-NC

Sulfur composites were prepared by the melt-diffusion method. In detail, sulfur and host materials (FeCo-NC, Co-NC and Fe-NC) were mixed at a ratio of 4:1, which were grounded in a mortar for 30 min. Then the mixture was put into a glass bottle and heated at 155 °C for 12 h to enable the diffusion of the sulfur substance into the host materials.

### 2.9. $\text{Li}_2\text{S}_6$ symmetric cell assembly and measurement

$\text{Li}_2\text{S}_6$  symmetrical cells were assembled in a glovebox filled with Ar atmosphere. 0.2  $\text{mol L}^{-1}$   $\text{Li}_2\text{S}_6$  solution was prepared by mixing  $\text{Li}_2\text{S}$  and sulfur with a molar ratio of 1:5 in the DME/1,3-dioxolane (DOL) solution containing 0.5  $\text{mol L}^{-1}$  LiTFSI and 0.5  $\text{mol L}^{-1}$   $\text{LiNO}_3$ . The FeCo-NC/CP, Co-NC/CP and Fe-NC/CP were prepared by dissolving 10 mg FeCo-NC, Co-NC or Fe-NC in 5 mL ethanol and dropping them evenly on the carbon paper, which enabled a mass loading of 0.5  $\text{mg cm}^{-2}$ . The two identical electrodes were assembled into a standard CR2032 coin cell with a Celgard 2400 membrane served as the separator. 40  $\mu\text{L}$  as-prepared  $\text{Li}_2\text{S}_6$  solution was used as the electrolyte. CV tests of symmetric cells were performed at a scan rate of 0.5 and 50  $\text{mV s}^{-1}$  with the

voltage ranging from  $-1$ – $1$  V.

### 2.10. PITT measurement

The coin cell for the PITT test was assembled using FeCo-NC/CP, Co-NC/CP and Fe-NC/CP as the working electrode and Li foil as the anode. 40  $\mu$ L of catholyte (0.2 mol L<sup>-1</sup> Li<sub>2</sub>S<sub>8</sub> dissolved in DOL/DME with 0.5 mol L<sup>-1</sup> LiTFSI and 0.5 mol L<sup>-1</sup> LiNO<sub>3</sub>) and 5  $\mu$ L of blank electrolyte were dropped onto the cathode and anode side, respectively. The PITT test was conducted on the PARSTAT 3000 A electrochemical workstation. The cell was potentiostatically discharged from the open voltage to 1.9 V and then charged to 2.5 V with 50.0 mV per interval.

### 2.11. Li<sub>2</sub>S nucleation tests

0.2 mol L<sup>-1</sup> Li<sub>2</sub>S<sub>8</sub> solution was prepared by dissolving Li<sub>2</sub>S and sulfur at a molar ratio of 1:7 in tetraglyme solution, followed by a vigorous stirring at 60 °C for 24 h. As-prepared FeCo-NC/CP, Co-NC/CP and Fe-NC/CP were employed as cathode, lithium foil as anode and Celgard 2400 membrane as the separator. 25  $\mu$ L Li<sub>2</sub>S<sub>8</sub> (0.2 mol L<sup>-1</sup>) electrolyte was added into the cathode and 25  $\mu$ L LiTFSI (0.5 mol L<sup>-1</sup>) was added into the anode side. The assembled cells were galvanostatically discharged to 2.06 V at 0.112 mA and kept potentiostatically at 2.05 V to obtain the current response as a function of time until the current decreased to below 10<sup>-5</sup> A.

### 2.12. Li<sub>2</sub>S<sub>4</sub> visualized adsorption tests

Li<sub>2</sub>S<sub>4</sub> solution with a concentration of 5 mmol L<sup>-1</sup> was prepared by mixing Li<sub>2</sub>S and sulfur in the 1,2-dimethoxyethane (DME) solution at a molar ratio of 1:3, followed by the continuous stirring until completely dissolved. Then, 5 mg FeCo-NC, Co-NC and Fe-NC were added to 2 mL as-prepared Li<sub>2</sub>S<sub>4</sub> solutions. The whole process was carried out in a glove box.

### 2.13. Assembling and testing of Li-S batteries

The standard CR2032 coin cells were assembled using S/FeCo-NC, S/Co-NC and S/Fe-NC as the cathode, Li foil as the anode and Celgard 2400 membrane as the separator. The electrolyte contained 0.5 M LiTFSI in a solvent mixture of DOL and DME (1:1 in volume) with 0.5 M LiNO<sub>3</sub>. The E/S ratio used in the coin cells with typical sulfur loading was 15  $\mu$ L mg<sup>-1</sup>. CV measurements at varied scan rates were carried out on the CHI660D electrochemical workstation. GCD tests and rate/cycling performance were conducted on a LAND battery testing system with a voltage range of 1.7–2.8 V (vs. Li/Li<sup>+</sup>).

### 2.14. Characterization

The crystal structures of products were characterized by XRD with a Bruker D8 Advance Diffractometer based on a Cu-K $\alpha$  radiation. Morphological micrographs and EDS maps were collected using a Hitachi SU8010 Scanning Electron Microscopy (SEM) and a Titan Themis Cubed G2300 Transmission Electron Microscopy (TEM). The aberration-corrected HAADF-STEM images were taken by a TEM (FEI Titan3 G2 60–300) equipped with double spherical aberration correctors. XPS measurements were conducted on an Escalab 250Xi Spectrophotometer using a monochromatic Al K $\alpha$  x-ray source. N<sub>2</sub> adsorption/desorption isotherms were obtained at 77 K on a Micromeritics Tristar II 3020 Accelerated Surface Area and Porosimetry System. SAC loading was analyzed by ICP-OES using an Optima 8000 equipment (Perkin Elmer).

### 2.15. Theoretical calculations

Theoretical calculations in this work were conducted using the

Quantum ESPRESSO package based on the density functional theory (DFT). The exchange-correlation potential was considered within the norm-conserving pseudopotentials and the Perdew-Burke-Ernzerhof functional. The slab models were built based on a 6  $\times$  6  $\times$  1 graphene model with a 15 Å thickness of the vacuum region along the (0 0 1) direction. Fe, Co, and N atom was substituted for C atom in the graphene. The Monkhorst-pack K-point grids were 5  $\times$  5  $\times$  1 in both structural relaxation and adsorption simulation. The lithium atom migration from Li<sub>2</sub>S on Fe-NC, Co-NC and FeCo-NC was simulated as the decomposition process. Charge density difference calculation was performed to evaluate the charge transfer during the reduction of sulfur.

## 3. Results and discussion

### 3.1. Electronic structural analysis and orbital interactions by DFT calculations

Fig. 1a illustrates a schematic diagram of our devised geminal-atom polysulfide mediator targeting selective catalysis in Li–S chemistry. To rationalize the design, density functional theory (DFT) calculations were carried out to study the nucleation (Li<sub>2</sub>S<sub>4</sub>  $\rightarrow$  Li<sub>2</sub>S) and dissociation (Li<sub>2</sub>S  $\rightarrow$  LiS) reactions of Li<sub>2</sub>S over the Fe-NC, Co-NC, and FeCo-NC. Firstly, the configurations of Fe-NC and Co-NC single-atomic and FeCo-NC geminal-atomic moieties were built (Fig. S1). Considering that nucleation of Li<sub>2</sub>S<sub>4</sub> to form Li<sub>2</sub>S is the rate-determining step in the SRR process, the adsorption configurations of reaction intermediates (Li<sub>2</sub>S<sub>4</sub>, Li<sub>2</sub>S<sub>2</sub>, and Li<sub>2</sub>S) with FeCo-NC, Fe-NC, and Co-NC were simulated (Fig. 1b; Figs. S2 and S3). As depicted in Fig. 1c, FeCo-NC has the lowest conversion barrier energy (0.46 eV) for the step of Li<sub>2</sub>S<sub>2</sub>  $\rightarrow$  Li<sub>2</sub>S, followed by those of Fe-NC (0.71 eV) and Co-NC (0.76 eV). Similarly, as for the Li<sub>2</sub>S<sub>4</sub>  $\rightarrow$  Li<sub>2</sub>S<sub>2</sub> step, FeCo-NC shows an obviously lower free energy change (0.21 eV) than the other two systems (0.31 eV on Fe-NC and 0.39 eV on Co-NC), indicating facilitated conversion from Li<sub>2</sub>S<sub>4</sub> to Li<sub>2</sub>S. The SER process is of equal importance in the bidirectional sulfur redox reaction. During the dissociation of Li<sub>2</sub>S, the initial delithiation (Li<sub>2</sub>S  $\rightarrow$  LiS + Li) plays a key role. The dissociation pathways and energy barriers were calculated to evaluate the decomposition process of Li<sub>2</sub>S. The Li<sub>2</sub>S dissociation configurations and pathways on FeCo-NC, Fe-NC, and Co-NC were modeled (Fig. 1d; Fig. S4). Fig. 1e exhibits that Co-NC and FeCo-NC have similar energy barriers, which is smaller than Fe-NC. This indicates that Co-NC and FeCo-NC have better catalytic activity for Li<sub>2</sub>S dissociation than Fe-NC.

Intriguingly, the above calculation results reveal the catalytic selectivity of the prevailing Fe and Co single-atom mediators to the sulfur redox reaction, which has been rarely probed to date. In this regard, Fe-NC is beneficial to the SRR process and Co-NC is in favor of boosting the SER process. Moreover, the electronic density of states (DOS) were calculated to reveal the electronic structures of Fe-NC, Co-NC, and FeCo-NC. Fig. 1f shows that all modelled materials present metallic features. In comparison, FeCo-NC exhibits the best electrical conductivity with dense electron distributions near the Fermi-level. Based on the partial DOS (PDOS) spectra, the main contributors to metallicity are 3d orbitals of Fe and Co, as well as 2p orbitals of N (Fig. S5). The high electrical conductivity favors facile electron transport and good electrocatalytic activity for Li–S battery. According to the intrinsic electronic structure, Fe-NC possesses a favorable adsorption capacity of Li<sub>2</sub>S, promoting the SRR process. In contrast, Fe-NC does not contribute to expediting the Li<sub>2</sub>S dissociation reaction, mainly pertaining to the excessively strong electrostatic interaction between Li<sub>2</sub>S and Fe-NC. As for the Co-NC mediator, its mediocre LiPS adsorptivity leads to the lowest Li<sub>2</sub>S dissociation barrier, which imparts the selective catalytic effect over SER. Based on these theoretical analysis, we conclude that geminal-atom synergy to render FeCo-NC mediator might allow optimal bidirectional electrocatalytic reaction kinetics of sulfur redox.

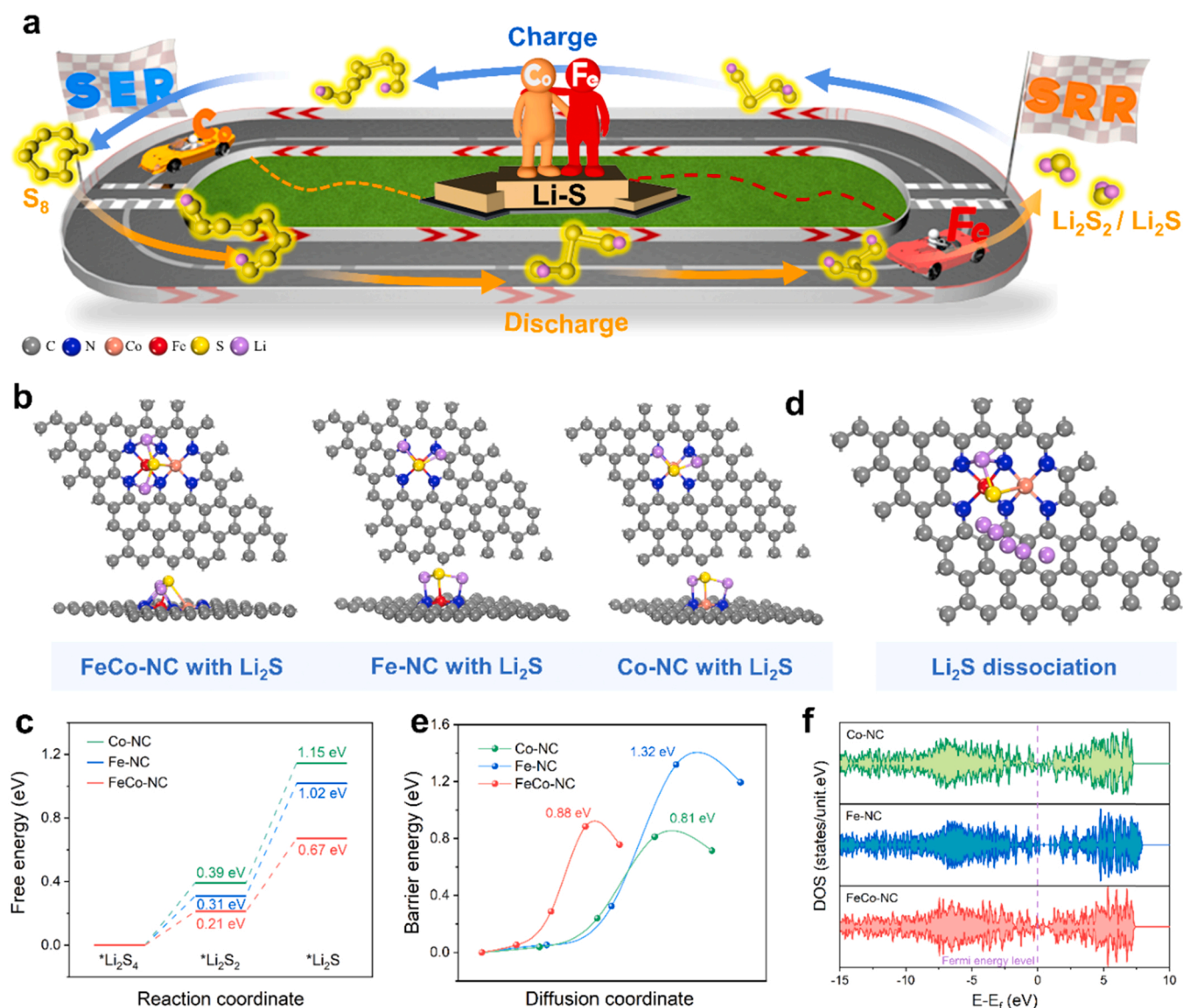


**Fig. 1.** Electronic structural analysis and orbital interactions by DFT calculations. (a) Illustration of the selective catalysis for designing Fe and Co based DACs for Li-S batteries. (b). Optimized structures of  $\text{Li}_2\text{S}$  absorbed on FeCo-NC, Fe-NC, and Co-NC. (c) Free energy of  $\text{Li}_2\text{S}$  nucleation. (d) Decomposition pathways of  $\text{Li}_2\text{S}$  on FeCo-NC. (e) Barrier energy of  $\text{Li}_2\text{S}$  dissociation. (f) Density of states of FeCo-NC, Fe-NC, and Co-NC.

### 3.2. Synthesis and characterization of the FeCo-NC

Fig. 2a depicts the synthetic procedure of the FeCo-NC. The desirable architecture of carbon support was realized by using a salt-confined synthetic route, which exhibits a 3D porous framework as sulfur host and abundant sites for accommodating Fe/Co atoms. In general, the ZnCo-ZIF was prepared by using the precursors of  $\text{Zn}(\text{NO}_3)_2 \cdot 6\text{H}_2\text{O}$ , Co  $(\text{NO}_3)_2 \cdot 6\text{H}_2\text{O}$  ( $\text{Zn}^{2+}:\text{Co}^{2+} = 40:1$ ) and 2-methylimidazole. ZnCo-ZIF crystals were evenly distributed in saturated NaCl solution by ultrasonic treatment (Fig. S6). NaCl@ZnCo-ZIF was then obtained by adding alcohol until NaCl was precipitated. The thus-derived mixture was subject to a thermal treatment under Ar ambient at 900 °C for 2 h, generating NaCl@Co-NC product with enriched nitrogen doping. The obtained powder was dosed by  $\text{FeSO}_4/1,10$ -phenanthroline and annealed at 700 °C to bring in Fe single atoms. Finally, acid etching was employed to simultaneously remove the NaCl and unwanted metal clusters, finally giving rise to the formation of FeCo-NC. Such a salt-confined synthetic route harvests certain advantages, including large scalability, good controllability and high metal atom loading.

The morphological information of as-prepared FeCo-NC was

inspected by scanning electron microscopy (SEM) and transmission electron microscopy (TEM). It is evident that the ZnCo-ZIF possesses a rhombic dodecahedral morphology with an average size of 800 nm (Figs. S7 and S8). SEM images show that the morphology of FeCo-NC and ZnCo-ZIF is consistent owing to the protective effect of NaCl template (Fig. 2b). Note that Fe-NC and Co-NC harvest homologous morphologies with FeCo-NC, which allows direct performance comparison of the different mediators (Fig. S9). The detailed porous structure of FeCo-NC is observed by TEM imaging (Fig. 2c; Fig. S10). Scanning TEM (STEM) observation and related energy dispersive X-ray spectroscopy (EDS) maps of FeCo-NC imply the homogeneous distribution of C, N, Co, and Fe elements over the rhombic dodecahedron (Fig. 2d and e). The distribution of elements in Co-NC and Fe-NC has similar characteristics (Figs. S11 and S12). The high-resolution TEM (HRTEM) view displays the typical porous carbon structure of the NC support (Fig. 2f; Fig. S13). The high-angle annular dark-field STEM (HAADF-STEM) inspections evidence the Fe and Co distributions at an atomic resolution of FeCo-NC. As depicted in Fig. 2f, the bright spots distributed within the image correspond to isolated Fe and Co atoms because of the superior atomic number contrast (Fig. 2g). It is noticeable that the isolated atoms exist in

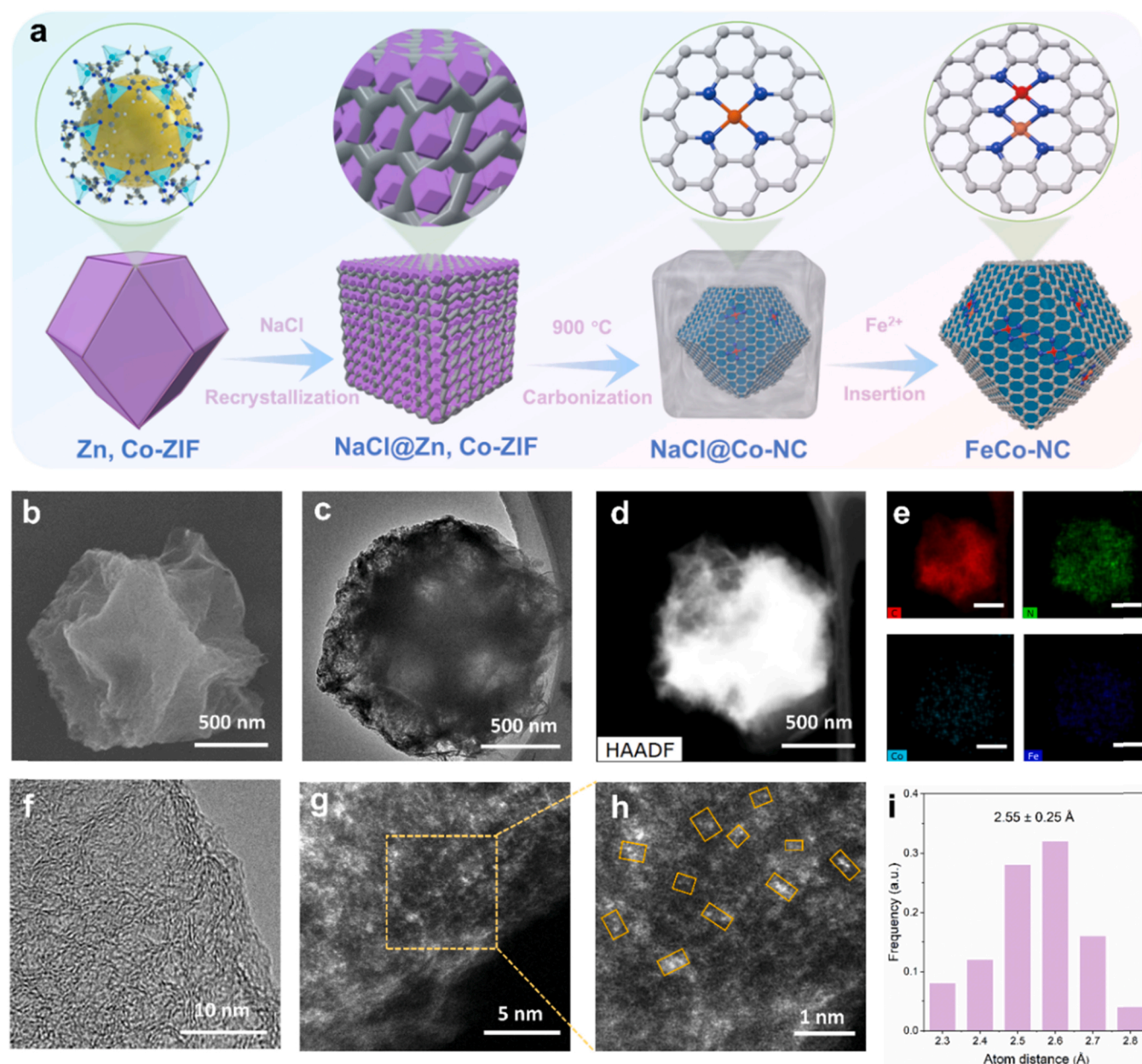


**Fig. 2.** Fabrication process and characterization of the FeCo-NC. (a) Schematic illustration of FeCo-NC synthesis. (b) SEM image of FeCo-NC. (c) TEM image of FeCo-NC. (d) HAADF-STEM image and (e) corresponding elemental maps of FeCo-NC. (f) HRTEM image of FeCo-NC. (g, h) HAADF-STEM image of FeCo-NC with representative geminal-atom pairs highlighted by yellow rectangles. (i) Statistical Fe and Co distances in the observed geminal-atom pairs.

the form of pairs (highlighted by yellow boxes), which could be considered as Fe/Co geminal-atom moieties (Fig. 2h). Furthermore, statistical analysis on the visible spatial distance of atom pairs shows the average value of  $2.55 \pm 0.25 \text{ \AA}$  (Fig. 2i). In contrast, a multitude of single bright spots could be observed in the HAADF-STEM images of Co-NC and Fe-NC, verifying the dispersed single-atomic features (Fig. S14).

### 3.3. Structural characterization of the as-prepared FeCo-NC

X-ray diffraction (XRD) patterns of three samples display two broad peaks located at  $\sim 24^\circ$  and  $44^\circ$ , which could be respectively assigned to the (002) and (101) planes of NC (Fig. 3a). No significant metal or metal oxide diffraction peaks were found because of atomic doping of Fe and Co, in good agreement with the TEM/HAADF-STEM characterization results. Moreover, N<sub>2</sub> adsorption/desorption measurement was performed to detect the surface area and pore characteristics (Fig. S15). The

Brunauer–Emmett–Teller (BET) result illustrates that the specific surface areas of FeCo-NC, Co-NC, and Fe-NC are 931.0, 1273.6 and 1234.2 m<sup>2</sup> g<sup>−1</sup>, respectively. Samples exhibit micropore- and mesopore-dominated pore size distribution, which would not only alleviate volume change upon electrochemical cycling but also enable high sulfur loadings. As a result, the sulfur content of S/FeCo-NC, S/Co-NC, and S/Fe-NC could reach  $\sim 80\%$  by thermogravimetric analysis (Fig. S16).

The surface states and chemical environments of FeCo-NC, Co-NC, and Fe-NC were disclosed by X-ray photoelectron spectroscopy (XPS). The full-scan spectrum corroborates the presence of C, N, Fe, and Co elements (Fig. S17). As depicted in the C 1s spectrum, all three samples show the existence of C–C, C–N, C=N and C–O bonding, respectively (Fig. S18). As depicted in N 1s spectra (Fig. 3b), the peaks at 398.5, 399.5, 400.9, 402.5, and 404.4 eV are assigned to pyridinic-N, M–N, pyrrolic-N, graphite-N, and oxidized-N, respectively [37]. Co 2p and Fe 2p spectra suggest that Co and Fe of FeCo-NC, Co-NC, and Fe-NC are in

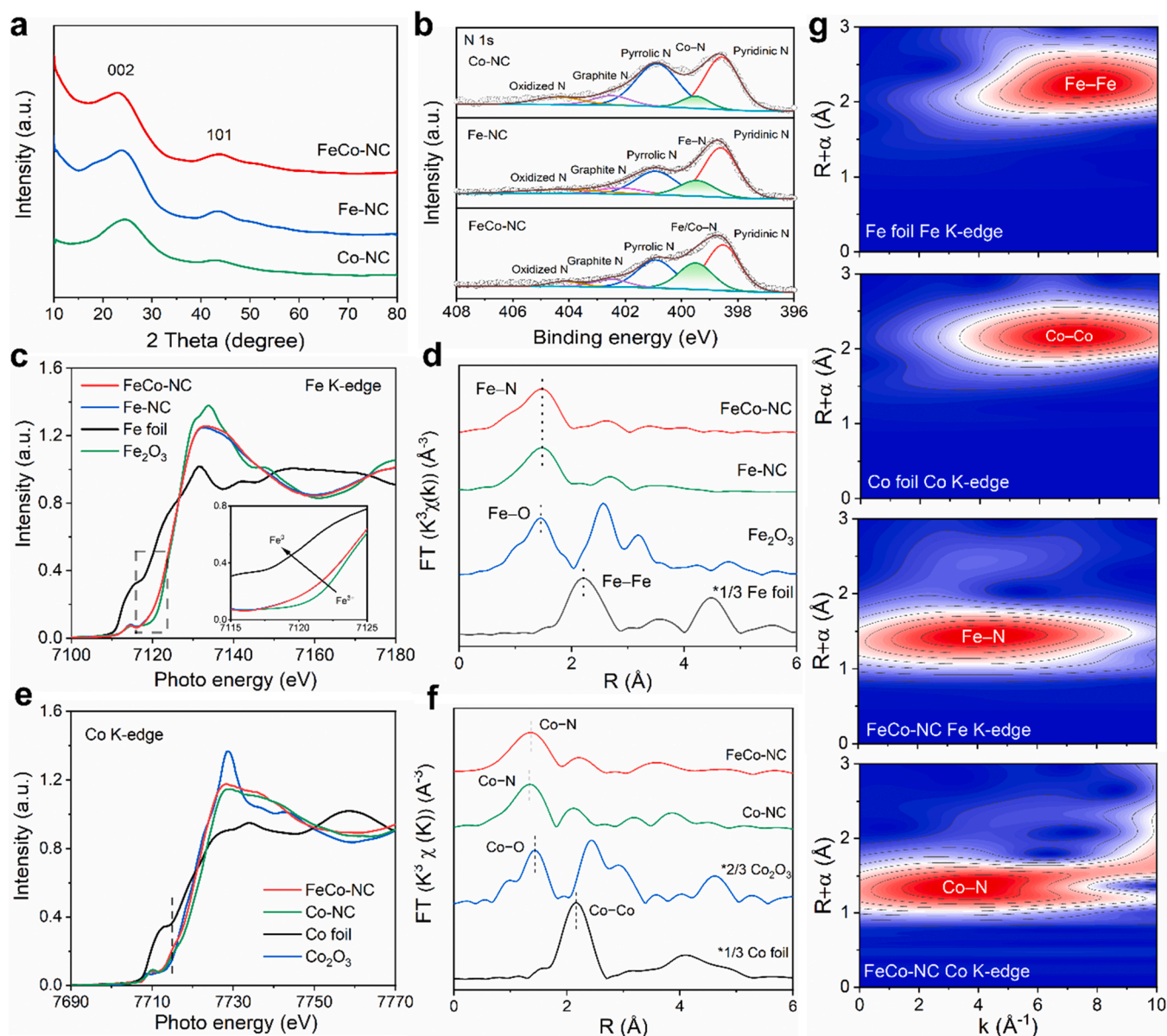


**Fig. 3.** Structural characterization of the as-prepared FeCo-NC, Fe-NC, and Co-NC. (a) XRD patterns of FeCo-NC, Fe-NC, and Co-NC. (b) High-resolution XPS N 1s spectra. (c) Fe K-edge XANES and (d) FT-EXAFS spectra of the FeCo-NC, Fe-NC, Fe foil, and  $\text{Fe}_2\text{O}_3$ . (e) Co K-edge XANES and (f) FT-EXAFS spectra of the FeCo-NC, Co-NC, Co foil, and  $\text{Co}_2\text{O}_3$ . (g) WT contour plots of Fe foil, Co foil, and FeCo-NC.

their oxidative states, indicative of the rare formation of metal clusters (Fig. S19). Inductively coupled plasma optical emission spectrometry (ICP-OES) measurement additionally reveals that metal content information, reaching ca. 3.5 wt% (Fe: 1.8 wt%; Co: 1.7 wt%) in FeCo-NC, 3.7 wt% in Fe-NC and 3.6 wt% in Co-NC (Table S1).

To gain a deeper understanding of the chemical state and coordination environment of Fe and Co atoms in the geminal-atom engineering, the FeCo-NC was characterized using the X-ray absorption near-edge structure (XANES) and extended X-ray absorption fine structure (EXAFS). Fig. 3c displays the Fe K-edge XANES spectra recorded for the FeCo-NC, Fe-NC, Fe foil and  $\text{Fe}_2\text{O}_3$ . The position in the absorption edge for FeCo-NC and Fe-NC located between Fe foil and  $\text{Fe}_2\text{O}_3$ , which proves that the valence of Fe in FeCo-NC and Fe-NC between 0 and +3 (Fig. 3c inset). As shown in Fig. 3d, the Fourier transform (FT)  $k^3$ -weighted EXAFS spectra of Fe K-edge show apparent the same peak of FeCo-NC and Fe-NC at 1.47 Å corresponding to the Fe-N coordination. Moreover, the Co K-edge XANES spectra of FeCo-NC and the corresponding reference samples reveal that the absorption edge position of Co in FeCo-

NC closes to that of Co-NC, indicating between 0 and +3 valence state (Fig. 3e). At the position of pre-edge peak 7715 eV, the valence state of FeCo-NC is slightly change than that of Co-NC because of the interaction of Co with Fe in the geminal-atom structure [38]. In response, a slight shift in the direction of higher average bond length is found in the position corresponding to the Co-N bond in the FT-EXAFS spectra, which proves the attraction of Fe atom to Co atom in the geminal-atom pair (Fig. 3f). In addition, the  $k^2$ -weighted  $k$ -space spectra of Fe and Co corresponding to EXAFS were fitted (Fig. S20). The wavelet transform (WT) EXAFS analysis with powerful resolution in both  $k$  and  $R$  spaces was performed to identify metal-N and metal-metal path (Fig. 3g; Fig. S21). The intensity maxima at  $7.7 \text{ Å}^{-1}$  in the WT plots of Fe foil is ascribed to the Fe-Fe bond and  $7.1 \text{ Å}^{-1}$  in the Co foil is Co-Co bond. The contour plots for FeCo-NC present WT-maximum at  $4.2 \text{ Å}^{-1}$  (Fe K-edge) and  $3.7 \text{ Å}^{-1}$  (Co K-edge), implying that only metal-N bond configurations exists in its atomic structure. In addition, the WT signals at  $3.8 \text{ Å}^{-1}$  and  $3.9 \text{ Å}^{-1}$  are derived from Fe-N and Co-N bond, showing that the Fe-NC and Co-NC are composed of atomically dispersed single-atom

sites with metal–N configurations.

### 3.4. Selective catalytic performance test

To probe the selective catalytic essence of Fe-NC, Co-NC and FeCo-NC with respect to the sulfur redox reaction, a series of electro-kinetic tests were carried out. As depicted in Fig. 4a–c, cyclic voltammetry (CV) profiles of the symmetric cells were collected in a  $\text{Li}_2\text{S}_6$  electrolyte

at a scan rate of  $0.5 \text{ mV s}^{-1}$ . All the cells show two pairs of redox peaks ( $a$  and  $b$ ;  $a_0$  and  $b_0$ ). Peak  $a$  reflects the reduction of  $\text{Li}_2\text{S}_6$  to  $\text{Li}_2\text{S}_4$  and peak  $b$  implies the reduction of  $\text{Li}_2\text{S}_4$  to  $\text{Li}_2\text{S}$ . The peak  $a_0$  and  $b_0$  represent the reversible oxidation process. Obviously, FeCo-NC/carbon paper (CP) harvests sharper redox peaks and smaller voltage polarization as compared with Fe-NC/CP and Co-NC/CP, indicative of the kinetically enhanced sulfur redox. Interestingly, the curves of Fe-NC/CP and Co-NC/CP exhibit weak symmetry due to their selective catalysis of

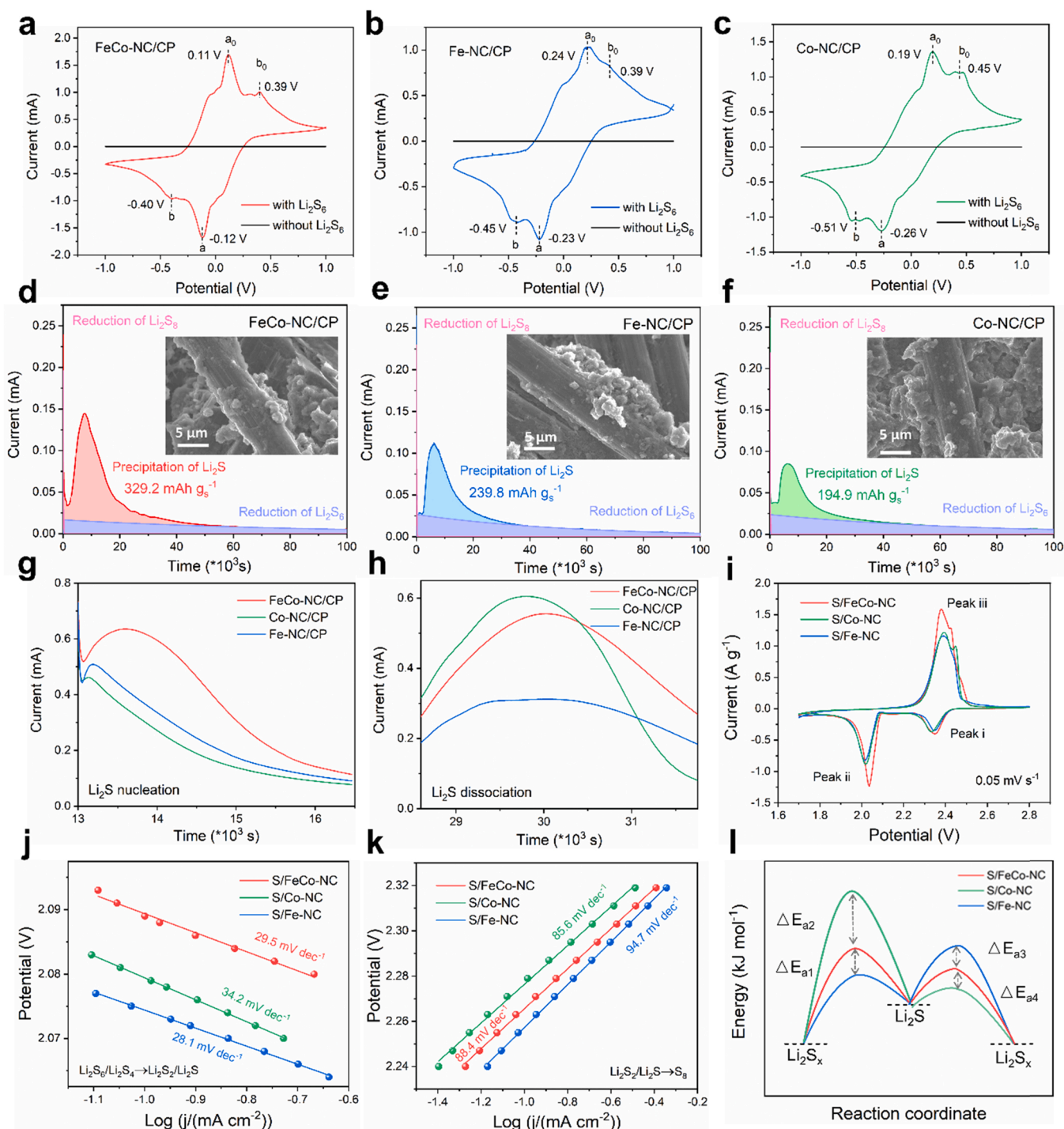


**Fig. 4.** Selective catalytic performance test. CV curves of (a) FeCo-NC/CP, (b) Fe-NC/CP, and (c) Co-NC/CP symmetric cells with the addition of  $\text{Li}_2\text{S}_6$  electrolyte at a scan rate of  $0.5 \text{ mV s}^{-1}$ . Potentiostatic discharge profiles of  $\text{Li}_2\text{S}_6$  solution on (d) FeCo-NC/CP, (e) Fe-NC/CP, and (f) Co-NC/CP, respectively. Inset: SEM images of precipitated  $\text{Li}_2\text{S}$ . Current response in the PITT test at the constant potentials of (g)  $2.0 \text{ V}$  in the discharge process and (h)  $2.4 \text{ V}$  in the charge process. (i) Typical CV curves of Li–S batteries S/FeCo-NC, S/Fe-NC, and S/Co-NC electrodes at  $0.05 \text{ mV s}^{-1}$ . Tafel plots for (j) the liquid–solid reduction process of  $\text{Li}_2\text{S}_6$  nucleation and (k) the solid–liquid oxidation process of  $\text{Li}_2\text{S}$  dissolution. (l) Activation energies of the precipitation and dissolution of  $\text{Li}_2\text{S}$ .

the sulfur redox process. Specifically, the reduction peak voltage polarization of Fe-NC/CP is significantly lower than that of Co-NC/CP, which proves that Fe-NC has better catalytic activity for SRR process. On the contrary, the Co-NC/CP oxidation peak voltage polarization is smaller than Fe-NC/CP, indicating a strong SER catalytic process. Therefore, FeCo-NC/CP exhibits rapid bidirectional sulfur redox kinetics because of the collective advantages. Likewise, a higher redox current response can also be detected on FeCo-NC/CP as compared to the remaining counterparts at a scan rate of  $50 \text{ mV s}^{-1}$  (Fig. S22). The electrochemical impedance spectroscopy (EIS) curves of symmetric cells show that catalyst FeCo-NC has the best LiPS transport capacity in Li-S system (Fig. S23).

To deepen the understanding of the  $\text{Li}_2\text{S}$  deposition process, the cells with  $\text{Li}_2\text{S}_8$  solution as the electrolyte were first discharged to 2.06 V and then potentiostatically discharge was performed at 2.05 V. The current response curve at 2.05 V were acquired, and the integral area corresponded to the nucleation capacity of  $\text{Li}_2\text{S}$  (Fig. 4d–f). It can be seen that the  $\text{Li}_2\text{S}$  deposition capacity ( $329.2 \text{ mAh g}^{-1}$ ) of FeCo-NC/CP is significantly higher than that of Fe-NC/CP ( $239.8 \text{ mAh g}^{-1}$ ) and Co-NC/CP ( $194.9 \text{ mAh g}^{-1}$ ). Meanwhile, SEM images further reveal the uniform deposition of  $\text{Li}_2\text{S}$  on the surface of FeCo-NC/CP (Fig. 4d inset), in contrast to the formation of plate-like  $\text{Li}_2\text{S}$  by Fe-NC/CP and Co-NC/CP (Fig. 4e and f inset). To further unravel the selective electrocatalysis toward bidirectional sulfur chemistry, the potentiostatic intermittent titration technique (PITT) measurement was carried out to monitor the nucleation and dissociation reactions of  $\text{Li}_2\text{S}$  in  $\text{Li}_2\text{S}_8$ -containing electrolytes. For liquid-solid conversion of  $\text{Li}_2\text{S}$  nucleation, the assembled battery was potentiostatically discharged from 2.25 V constant potential to 1.8 V at 50.0 mV intervals. The sharp current peak at 2.0 V indicates the precipitation of solid-phase  $\text{Li}_2\text{S}$  from liquid-phase LiPSs (Fig. 4g). Obviously, FeCo-NC/CP exhibits the largest deposition current response and integral area representing excellent  $\text{Li}_2\text{S}$  nucleation kinetics. Similarly, Fe-NC/CP has a greater catalytic capacity than Co-NC/CP in SRR process. Similarly, the dissociation of  $\text{Li}_2\text{S}$  was studied by statically charging the battery from 2.2 V to 2.5 V at 100.0 mV intervals by potential, and the peak current at 2.4 V representing the amount of dissociation (Fig. 4h). The high SER catalytic capacity of FeCo-NC and Co-NC is reflected in their much higher peak current than Fe-NC because of the selective catalytic of Co-NC. Overall, FeCo-NC harvests higher response current and deposition/dissolution capacity, further corroborating the promoted electrocatalytic effect on the dual-directional sulfur redox chemistry.

In the electrochemical behavior of Li-S batteries, the redox process during the charging and discharging is represented in the peak of the CV profile at a scan rate of  $0.05 \text{ mV s}^{-1}$  (Fig. 4i). During the discharge process, two featured cathodic peaks appeared at 2.3 ~ 2.4 V (peak i) and 1.9 ~ 2.1 V (peak ii), which are attributed to the formation of soluble LiPSs and insoluble  $\text{Li}_2\text{S}$ , respectively. The anodic peak is located in the range of 2.3 ~ 2.6 V (peak iii), corresponding to the decomposition of  $\text{Li}_2\text{S}$  during the charge process. It is worth-noting that S/FeCo-NC electrode has a greater current response and lower voltage polarization than other counterparts, which originates from the superior electrocatalytic activity of synergistic Fe and Co atoms. Meanwhile, the CV profiles of S/FeCo-NC electrode with different scan rates from 0.1 to  $0.5 \text{ mV s}^{-1}$  indicate the efficient ion transport capability (Fig. S24). The variable-temperature (30–50 °C) CV test verifies the catalytic stability of FeCo-NC catalyst in the sulfur redox electrochemical process (Fig. S25) [39].

The Tafel slopes of reduction (from  $\text{S}_8$  to  $\text{Li}_2\text{S}_n$  and  $\text{Li}_2\text{S}_n$  to  $\text{Li}_2\text{S}$ ) and oxidation (from  $\text{S}_8$  to  $\text{Li}_2\text{S}$ ) were further derived to quantify the electrocatalytic effect. The solid-liquid transition during sulfur reduction ( $\text{S}_8$  to  $\text{Li}_2\text{S}_6/\text{Li}_2\text{S}_4$ ) clearly shows that S/FeCo-NC has the smallest Tafel slope, proving the fastest kinetics (Fig. S26). More importantly, the selective catalytic effect of catalysts in SRR and SER processes was further confirmed. As shown in Fig. 4j, S/Fe-NC exhibits the smallest Tafel slope ( $28.1 \text{ mV dec}^{-1}$ ) in the SRR determination step, while S/FeCo-NC

( $29.5 \text{ mV dec}^{-1}$ ) is also smaller than the slope of S/Co-NC ( $34.2 \text{ mV dec}^{-1}$ ). On the contrary, S/Co-NC ( $85.6 \text{ mV dec}^{-1}$ ) exhibited the smallest Tafel slope than that of S/FeCo-NC ( $88.4 \text{ mV dec}^{-1}$ ) and S/Fe-NC ( $94.7 \text{ mV dec}^{-1}$ ) during the SER process, demonstrating the advantage of weak polysulfide adsorption in the  $\text{Li}_2\text{S}$  deposition process (Fig. 4k). Enhanced polysulfide kinetics can be quantified as the activation energy ( $E_a$ ) obtained by Tafel plots fitting [40]. The activation energy difference of each reaction process was directly compared, according to the activation energy calculation equation (1):  $E_a = E_a^0 + azF\varphi_{\text{cathode}}(\text{Ox}|\text{Red})_{\text{IR}}$ , where  $E_a$  is the activation energy of reduction process,  $E_a^0$  is the intrinsic activation energy,  $a$  is the symmetry coefficient,  $z$  is the number of charge transfer,  $F$  is the Faraday's constant,  $\varphi_{\text{cathode}}(\text{Ox}|\text{Red})_{\text{IR}}$  is the irreversible potential during cycling. In the Tafel process, the equation simplifies to (2):  $E_a = E_a^0 - \frac{RT}{b}\varphi_{\text{cathode}}(\text{Ox}|\text{Red})_{\text{IR}}$ , where  $b$  is the slope of Tafel curve. Fig. 4l shows the relative difference of activation energy of the three systems during nucleation and decomposition of  $\text{Li}_2\text{S}$ , and the calculated parameters are reflected in Table S2. Owing to the combination of S/Fe-NC and S/Co-NC selective catalytic ability for SRR and SER processes, S/FeCo-NC exhibits holistic catalytic performance, which has been shown to be better for Li-S catalysis in theoretical calculations. In addition, S/FeCo-NC demonstrates the smallest  $E_a$  value for the reduction of  $\text{S}_8$  to  $\text{Li}_2\text{S}_x$ , representing excellent solid-liquid catalytic ability during the SRR process (Fig. S27). All these results cooperatively identify the significantly boosted bidirectional sulfur redox kinetics by FeCo-NC with geminal-atom coordination geometry.

### 3.5. Electrochemical performance of Li-S batteries

To comprehensively reveal the electrocatalytic effect upon enhancing electrochemical performance, FeCo-NC, Co-NC, and Fe-NC were employed as the sulfur hosts in typical Li-S coin-type cells. Fig. 5a displays the galvanostatic charge/discharge (GCD) curves of different electrodes with S/FeCo-NC, S/Co-NC, and S/Fe-NC at 0.2 C ( $1.0 \text{ C} = 1675 \text{ mA g}^{-1}$ ). The S/FeCo-NC electrode delivers a higher capacity and the lowest voltage gap compared to the other two electrodes, verifying the excellent reaction kinetics of polysulfide conversion. Rate performances of S/FeCo-NC, S/Co-NC and S/Fe-NC electrodes were evaluated under different current densities from 0.2 C through 3.0 C and back to 0.2 C (Fig. 5b). The S/FeCo-NC electrode demonstrates superior capacities of 1303.9, 1103.6, 1003.4, 871.1 and  $775.9 \text{ mAh g}^{-1}$  at 0.2, 0.5, 1.0, 2.0 and 3.0 C, respectively. When the current density returns to 0.2 C, a high capacity of  $1250.2 \text{ mAh g}^{-1}$  can be restored, demonstrating good electrochemical reversibility. The corresponding GCD curve is shown in Fig. 5c, and the S/FeCo-NC electrode has a stable discharge platform at each current density. However, the discharge platforms of S/Co-NC and S/Fe-NC are almost lost under high-rate conditions (Fig. S28). It is evident that the specific capacities of S/FeCo-NC exhibit a prominent advantage over those of S/Co-NC and S/Fe-NC electrodes. Fig. 5d displays the cycling performances of Li-S batteries based on S/FeCo-NC, S/Co-NC, and S/Fe-NC electrodes at 0.2 C. The S/FeCo-NC electrode enables an initial capacity of  $1138.5 \text{ mAh g}^{-1}$  and maintains a discharge capacity of  $1122.6 \text{ mAh g}^{-1}$  after 100 cycles, accompanied by a capacity retention rate of 98.6%. In contrast, the S/Co-NC and S/Fe-NC electrodes acquire discharge capacity of  $1017.4 \text{ mAh g}^{-1}$  and  $982 \text{ mAh g}^{-1}$  with low corresponding capacity retention after 100 cycles. Even at a high current density of 3.0 C, S/FeCo-NC electrode still sustains a stable cycling operation with a low capacity decay rate of 0.033% per cycle after 2000 cycles, outperforming S/Co-NC and S/Fe-NC counterparts. Note that the electrochemical performances of S/FeCo-NC electrode compare favorably with previously reported Li-S battery counterparts employing geminal-atom catalyst mediators (Fig. 5f; Table S3). Optimizing the electrochemical performance under high sulfur loading is essential for the development of Li-S batteries for practical scene. Fig. 5g shows a stable cycling performance of examined

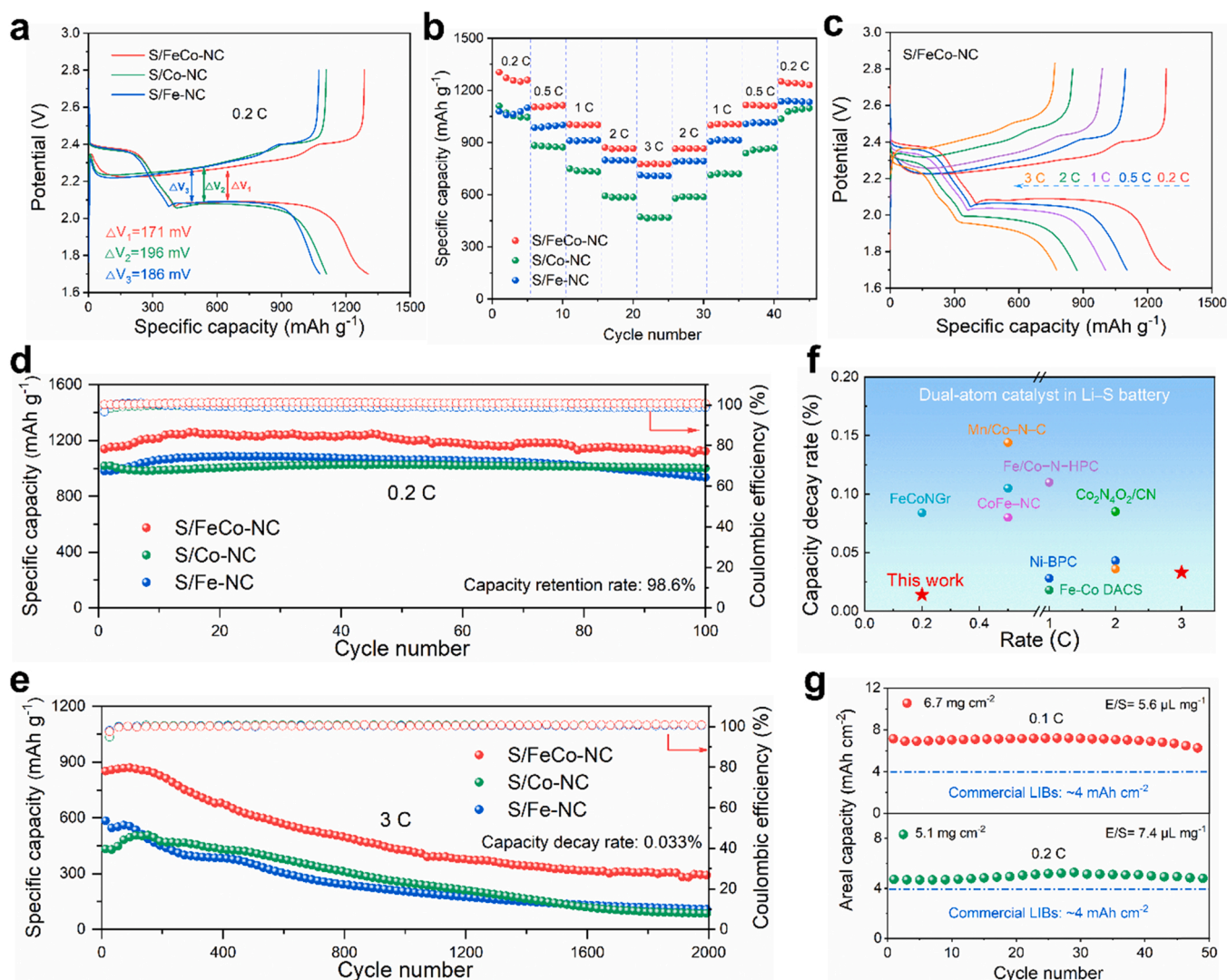


**Fig. 5.** Electrochemical performance of Li-S batteries. (a) GCD profiles at 0.2 C of S/FeCo-NC, S/Fe-NC, and S/Co-NC electrodes. (b) Rate performances and (c) corresponding GCD profiles of S/FeCo-NC, S/Fe-NC, and S/Co-NC electrodes. (d) Cycling performance at 0.2 C for 100 cycles. (e) Cycling performance of S/FeCo-NC, S/Fe-NC, and S/Co-NC electrodes at 3 C for 2000 cycles. (f) Comparison of capacity decay rate between this work and previously reported studies with various DACs. (g) Cycling performance of S/FeCo-NC electrode with a sulfur loading of 6.7 mg cm<sup>-2</sup> at 0.1 C and 5.1 mg cm<sup>-2</sup> at 0.2 C.

electrodes at the high sulfur loading. S/FeCo-NC electrode with a sulfur loading of 5.1 mg cm<sup>-2</sup> manifests an areal capacity of 4.72 mAh cm<sup>-2</sup> at 0.2 C with almost no capacity decay after 50 cycles. When the sulfur loading reaches 6.7 mg cm<sup>-2</sup>, it harvests an excellent initial areal capacity of 7.13 mAh cm<sup>-2</sup> and maintains 6.24 mAh cm<sup>-2</sup> even at 0.1 C after 50 cycles, transcending the typical areal capacity of commercial Li-ion battery (4.0 mAh cm<sup>-2</sup>). The corresponding GCD curve shows a stable discharge plateau, indicating S/FeCo-NC electrode excellent cycling ability under the high sulfur loading (Fig. S29). The low electrolyte/sulfur (E/S) ratio is another essential factor in achieving high energy density Li-S batteries. In this sense, the cell performance under an E/S ratio 4  $\mu$ L mg<sup>-1</sup> was tested at sulfur loadings of 5.7 mg cm<sup>-2</sup> at 0.1 C. The Li-S battery supported by the S/FeCo-NC electrode has a stable cycle of 100 cycles (Fig. S30).

### 3.6. DFT calculations and in situ characterizations

To further explore the role of sulfur chemistry of FeCo-NC, DFT calculation was carried out to investigate the influence of coordination environment on sulfur reaction kinetics. The charge transfer calculations were conducted by the charge density difference and Bader charge

analysis. Fig. 6a exhibits that the electron transfer between FeCo-NC and Li<sub>2</sub>S is 1.28 e<sup>-</sup>, larger than that of Fe-NC (1.22 e<sup>-</sup>) and Co-NC (1.07 e<sup>-</sup>). Similarly, the number of electrons transferred from S atoms in Li<sub>2</sub>S<sub>4</sub> to FeCo-NC are 0.62, 0.56, 0.24 and 0.10 e<sup>-</sup>, respectively. Those numbers are all larger than that of Fe-NC and Co-NC. The smooth electron transfer can facilitate the conversion process and improve the catalytic activity. Besides, the PDOS was calculated to unveil the interaction between FeCo-NC, Fe-NC, Co-NC and Li<sub>2</sub>S<sub>4</sub>, Li<sub>2</sub>S. Fig. 6b exhibit that 3d orbitals of Fe and Co in FeCo-NC and 2p orbitals of S in Li<sub>2</sub>S<sub>4</sub> have larger overlap nearby the Fermi-level than that of Fe-NC and Co-NC, which indicates the optimal d-p orbital hybrid state of FeCo-NC and Li<sub>2</sub>S<sub>4</sub>. Similarly, FeCo-NC and Li<sub>2</sub>S also show an optimal orbital hybridization compared to other structures (Fig. S31). The combination of Fe and Co enhance the electron transfer process to improve conversion process of LiPSs.

From an experimental point of view, it is necessary to probe that the adsorption manner and catalytic effect between FeCo-NC and LiPSs. To investigate the affinity of FeCo-NC with LiPSs, 5 mmol L<sup>-1</sup> Li<sub>2</sub>S<sub>4</sub> solution was prepared for visualized detection and UV-vis spectroscopy analysis (Fig. 6c). As shown in Fig. 6c inset, the Li<sub>2</sub>S<sub>4</sub> solution with the addition of FeCo-NC decolorizes after 3 h, indicating that it has a good adsorption effect on LiPSs and aids to further accelerate their conversion reaction.

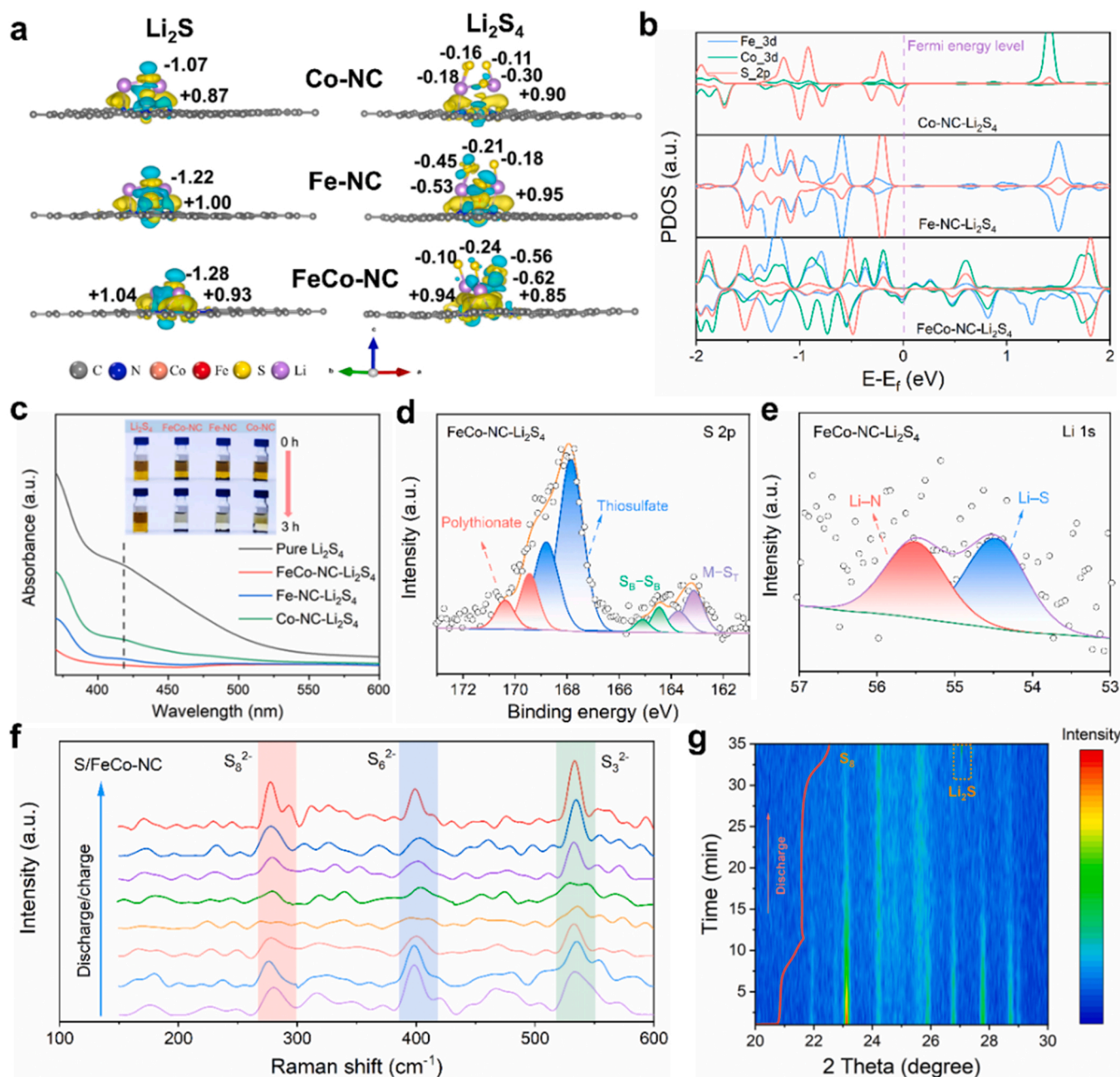


**Fig. 6.** DFT calculations and in situ characterizations of Li-S batteries. (a) Charge density difference of  $\text{Li}_2\text{S}$  and  $\text{Li}_2\text{S}_4$  adsorption. The upper, middle and down are on Co-NC, Fe-NC and FeCo-NC, respectively. The yellow and cyan areas represent the increased and decreased charges, respectively. (b) PDOS of  $\text{Li}_2\text{S}_4$  adsorbed on Fe-NC, Co-NC and FeCo-NC. (c) UV-vis absorption spectra in  $5 \text{ mmol L}^{-1}$   $\text{Li}_2\text{S}_4$  solution. Inset: Digital photo of visualized adsorption tests. XPS (d) S 2p spectrum and (e) Li 1s spectrum of FeCo-NC adsorbed  $\text{Li}_2\text{S}_4$  after 3 h. (f) Operando Raman spectra of the electrolyte with S/FeCo-NC electrode during the first cycle at a scan rate of  $0.2 \text{ mV s}^{-1}$ . (g) In situ XRD patterns of the S/FeCo-NC electrode during the first discharge process.

Meanwhile, Fe-NC exhibits stronger adsorption capacity compared with Co-NC due to its stronger  $d$ - $p$  orbital hybridization and selective catalysis capability, which conclusion is consistent with previous experiments. As for the UV-vis spectroscopy test, the  $\text{Li}_2\text{S}_4$  solution mixed with the FeCo-NC exhibits the weakest peak, further indicative of the strongest adsorption ability. To further understand its catalytic mechanism, the XPS results for adsorption products were also collected. As shown in Fig. 6d and Fig. S32, the S 2p spectrum upon the adsorption test could be divided into four contributions at 163.1/163.7, 164.5/165.1, 167.8/168.8, and 169.4/170.3 eV, which correspond to the terminal sulfur ( $\text{S}_7^{1-}$ ), bridged sulfur ( $\text{S}_6^{0}$ ), thiosulfate, and polythionate species, respectively [41]. The peak at 54.5 eV and 55.5 eV in the Li 1s spectrum of FeCo-NC- $\text{Li}_2\text{S}_4$  can be assigned to the Li-S and Li-N bonding (Fig. 6e),

suggesting the strong chemical anchoring between active N sites in FeCo-NC and the terminal Li atoms in  $\text{Li}_2\text{S}_4$  [42]. These results reveal that Lewis acid-base interaction exists between FeCo-NC and LiPSs, accordingly enhancing the capture and anchor of LiPSs.

Operando Raman spectroscopy and in situ XRD analysis were employed to offer insight into the catalytic effect of FeCo-NC during the charging/discharging of Li-S batteries [43–46]. Fig. 6f shows the collection of operando Raman spectra at a scan rate of  $0.2 \text{ mV s}^{-1}$  during the first full CV cycling. As for S/FeCo-NC electrode, Raman intensities of  $\text{S}_8^{2-}$ ,  $\text{S}_6^{2-}$  and  $\text{S}_3^{2-}$  peaks gradually decline in the discharge process and regenerate during charging, revealing the LiPS trapping and catalyzing ability of mediators. In situ XRD measurement was further carried out to witness the efficient SRR conversion during the first discharge process.

As shown in Fig. 6g, once the SRR process commences (open circuit voltage, OCV), the  $\alpha$ -S<sub>8</sub> crystal peaks at 23° (JCPDS 008-0247) and then weakens during the discharging. At the end of the discharge plateau (2.1 V), the peak at ~27° belongs to Li<sub>2</sub>S (JCPDS 023-0369) gradually appears and intensifies due to the liquid-solid conversion process of LiPSs, which indicates the efficient solid-liquid-solid phase conversion process of Li-S batteries with S/FeCo-NC electrode. These in situ characterizations results further demonstrate the efficient catalytic ability of FeCo-NC in Li-S batteries.

#### 4. Conclusion

In summary, we design a multifunctional FeCo-NC geminal-atom catalyst by means of salt-confined strategy for Li-S batteries, which is coupled by a single atom of selective catalysis and showcases an impressive electrocatalytic effect in promoting bidirectional sulfur redox chemistry. The selective catalytic ability of Fe to SRR and Co to SER endows the FeCo-NC efficient polysulfide management ability. Furthermore, electro-kinetic analysis and theoretical calculations reveal that the FeCo-NC can concurrently accelerate the Li<sub>2</sub>S nucleation and dissociation process, thereby enabling favorable bidirectional electrocatalysis. As a result, the S/FeCo-NC can harvest excellent areal capacity of 7.13 mAh cm<sup>-2</sup> with a high sulfur loading of 6.7 mg cm<sup>-2</sup>. This work provides a new avenue for designing robust mediators for Li-S batteries through selective catalysis in a practical manner.

#### CRedit authorship contribution statement

**Yifan Ding:** Data curation, Investigation, Formal analysis, Writing – original draft. **Tianran Yan:** Formal analysis, Project administration, Resources, Writing – original draft. **Jianghua Wu:** Formal analysis, Validation. **Meng Tian:** Investigation, Software, Writing – original draft. **Miaoyu Lu:** Investigation, Methodology. **Conglei Xu:** Investigation, Validation. **Jiayi Gu:** Formal analysis. **Haorui Zhao:** Investigation. **Yifei Wang:** Resources, Validation, Supervision, Writing – review & editing. **Xiaoqing Pan:** Formal analysis, Supervision. **Shi Xue Dou:** Formal analysis, Supervision, Writing – review & editing. **Liang Zhang:** Project administration, Validation, Resources, Supervision. **Jingyu Sun:** Conceptualization, Project administration, Supervision, Funding acquisition, Writing – review & editing.

#### Declaration of Competing Interest

The authors declare that they have no known competing financial interests or personal relationships that could have appeared to influence the work reported in this paper.

#### Data availability

Data will be made available on request.

#### Acknowledgements

Y.F.D., T.R.Y. and J.H.W. contributed equally to this work. This work was supported by the National Natural Science Foundation of China (22179089, 52000004), Science Fund for Distinguished Young Scholars of Jiangsu Province (BK20211503), and Postgraduate Research & Practice Innovation Program of Jiangsu Province (KYCX23\_3245). The authors acknowledge the support from Suzhou Key Laboratory for Advanced Carbon Materials and Wearable Energy Technologies, Suzhou, China.

#### Appendix A. Supporting information

Supplementary data associated with this article can be found in the online version at [doi:10.1016/j.apcatb.2023.123553](https://doi.org/10.1016/j.apcatb.2023.123553).

#### References

- [1] X. Ji, K.T. Lee, L.F. Nazar, A highly ordered nanostructured carbon-sulphur cathode for lithium-sulphur batteries, *Nat. Mater.* 8 (2009) 500–506.
- [2] P.G. Bruce, S.A. Freunberger, L.J. Hardwick, J.-M. Tarascon, Li–O<sub>2</sub> and Li–S batteries with high energy storage, *Nat. Mater.* 11 (2012) 19–29.
- [3] A. Manthiram, Y. Fu, S.-H. Chung, C. Zu, Y.-S. Su, Rechargeable lithium-sulfur batteries, *Chem. Rev.* 114 (2014) 11751–11787.
- [4] S.-H. Chung, A. Manthiram, Current Status and Future Prospects of Metal-Sulfur Batteries, *Adv. Mater.* 31 (2019) 1901125.
- [5] A. Bhargav, J. He, A. Gupta, A. Manthiram, Lithium-sulfur batteries: attaining the critical metrics, *Joule* 4 (2020) 285–291.
- [6] G. Zhou, H. Chen, Y. Cui, Formulating energy density for designing practical lithium-sulfur batteries, *Nat. Energy* 7 (2022) 312–319.
- [7] X. Liang, C. Hart, Q. Pang, A. Garsuch, T. Weiss, L.F. Nazar, A highly efficient polysulfide mediator for lithium-sulfur batteries, *Nat. Commun.* 6 (2015) 5682.
- [8] G. Li, S. Wang, Y. Zhang, M. Li, Z. Chen, J. Lu, Revisiting the role of polysulfides in lithium-sulfur batteries, *Adv. Mater.* 30 (2018) 1705590.
- [9] M. Jana, R. Xu, X.-B. Cheng, J.S. Yeon, J.M. Park, J.-Q. Huang, Q. Zhang, H.S. Park, Rational design of two-dimensional nanomaterials for lithium-sulfur batteries, *Energy Environ. Sci.* 13 (2020) 1049–1075.
- [10] Z. Shen, X. Jin, J. Tian, M. Li, Y. Yuan, S. Zhang, S. Fang, X. Fan, W. Xu, H. Lu, J. Lu, H. Zhang, Cation-doped ZnS catalysts for polysulfide conversion in lithium-sulfur batteries, *Nat. Catal.* 5 (2022) 555–563.
- [11] L. Peng, Z. Wei, C. Wan, J. Li, Z. Chen, D. Zhu, D. Baumann, H. Liu, C.S. Allen, X. Xu, A.I. Kirkland, I. Shakir, Z. Almutairi, S. Tolbert, B. Dunn, Y. Huang, P. Sautet, X. Duan, A fundamental look at electrocatalytic sulfur reduction reaction, *Nat. Catal.* 3 (2020) 762–770.
- [12] R. Wang, C. Luo, T. Wang, G. Zhou, Y. Deng, Y. He, Q. Zhang, F. Kang, W. Lv, Q.-H. Yang, Bidirectional Catalysts for Liquid-Solid Redox Conversion in Lithium-Sulfur Batteries, *Adv. Mater.* 32 (2020) 2000315.
- [13] L. Zhou, D.L. Danilov, F. Qiao, J. Wang, H. Li, R.-A. Eichel, P.H.L. Notten, Sulfur Reduction Reaction in Lithium-Sulfur Batteries: Mechanisms, Catalysts, and Characterization, *Adv. Energy Mater.* 12 (2022) 2202094.
- [14] J. Lei, X.X. Fan, T. Liu, P. Xu, Q. Hou, K. Li, R.M. Yuan, M.S. Zheng, Q.F. Dong, J. J. Chen, Single-dispersed polyoxometalate clusters embedded on multilayer graphene as a bifunctional electrocatalyst for efficient Li-S batteries, *Nat. Commun.* 13 (2022) 202.
- [15] W. Yao, C. Tian, C. Yang, J. Xu, Y. Meng, I. Manke, N. Chen, Z. Wu, L. Zhan, Y. Wang, R. Chen, P-Doped NiTe<sub>2</sub> with Te-vacancies in lithium-sulfur batteries prevents shuttling and promotes polysulfide conversion, *Adv. Mater.* 34 (2022) 2106370.
- [16] Y. Ding, Z. Shi, Y. Sun, J. Wu, X. Pan, J. Sun, Steering bidirectional sulfur redox via geometric/electronic mediator comodulation for Li-S batteries, *ACS Nano* 17 (2023) 6002–6010.
- [17] X. Zhang, T. Yang, Y. Zhang, X. Wang, J. Wang, Y. Li, A. Yu, X. Wang, Z. Chen, Single zinc atom aggregates: synergetic interaction to boost fast polysulfide conversion in lithium-sulfur batteries, *Adv. Mater.* 35 (2023) 2208470.
- [18] J. Cai, Z. Sun, W. Cai, N. Wei, Y. Fan, Z. Liu, Q. Zhang, J. Sun, A. Robust, Ternary Heterostructured Electrocatalyst with Conformal Graphene Chainmail for Expediting Bi-Directional Sulfur Redox in Li-S Batteries, *Adv. Funct. Mater.* 31 (2021) 2100586.
- [19] Z. Shi, Y. Ding, Q. Zhang, J. Sun, Electrocatalyst Modulation toward Bidirectional Sulfur Redox in Li-S Batteries: From Strategic Probing to Mechanistic Understanding, *Adv. Energy Mater.* 12 (2022) 2201056.
- [20] J.-L. Yang, P. Yang, D.-Q. Cai, Z. Wang, H.J. Fan, Atomically Dispersed Fe–N<sub>4</sub> and Ni–N<sub>4</sub> Independent Sites Enable Bidirectional Sulfur Redox Electrocatalysis, *Nano Lett.* 23 (2023) 4000–4007.
- [21] Z. Shi, Z. Sun, J. Cai, X. Yang, C. Wei, M. Wang, Y. Ding, J. Sun, Manipulating Electrocatalytic Li<sub>2</sub>S Redox via Selective Geminal-Defect Engineering for Li-S Batteries, *Adv. Mater.* 33 (2021) 2103050.
- [22] S. Li, J. Lin, B. Chang, D. Yang, D.-Y. Wu, J. Wang, W. Zhou, H. Liu, S. Sun, L. Zhang, Implanting single-atom N<sub>2</sub>-Fe-B<sub>2</sub> catalytic sites in carbon hosts to stabilize high-loading and lean-electrolyte lithium-sulfur batteries, *Energy Storage Mater.* 55 (2023) 94–104.
- [23] J. Chen, H. Li, C. Fan, Q. Meng, Y. Tang, X. Qiu, G. Fu, T. Ma, Geminal Single-Atomic Ni–N<sub>4</sub> and Fe–N<sub>4</sub> Sites Constructing Janus Hollow Graphene for Selective Oxygen Electrocatalysis, *Adv. Mater.* 32 (2020) 2003134.
- [24] M. Chen, J. Li, W. Xue, S. Wang, J. Han, Y. Wei, D. Mei, Y. Li, J. Yu, Unveiling Secondary-Ion-Promoted Catalytic Properties of Cu-SZ-13 Zeolites for Selective Catalytic Reduction of NO<sub>x</sub>, *J. Am. Chem. Soc.* 144 (2022) 12816–12824.
- [25] B. Yang, L. Chen, S. Xue, H. Sun, K. Feng, Y. Chen, X. Zhang, L. Xiao, Y. Qin, J. Zhong, Z. Deng, Y. Jiao, Y. Peng, Electrocatalytic CO<sub>2</sub> reduction to alcohols by modulating the molecular geometry and Cu coordination in bicentric copper complexes, *Nat. Commun.* 13 (2022) 5122.
- [26] W. Hua, H. Li, C. Pei, J. Xia, Y. Sun, C. Zhang, W. Lv, Y. Tao, Y. Jiao, B. Zhang, S.-Z. Qiao, Y. Wan, Q.-H. Yang, Selective Catalysis Remedies Polysulfide Shuttling in Lithium-Sulfur Batteries, *Adv. Mater.* 33 (2021) 2101006.
- [27] Y. Wang, J. Mao, X. Meng, L. Yu, D. Deng, X. Bao, Catalysis with two-dimensional materials confining single atoms: concept, design, and applications, *Chem. Rev.* 119 (2019) 1806–1854.
- [28] W. Guo, Z. Wang, X. Wang, Y. Wu, General design concept for single-atom catalysts toward heterogeneous catalysis, *Adv. Mater.* 33 (2021) 2004287.
- [29] Y. Ding, Q. Cheng, J. Wu, T. Yan, Z. Shi, M. Wang, D. Yang, P. Wang, L. Zhang, J. Sun, Enhanced Geminal-Directional Sulfur Redox via a Biotemplated Single-

- Atomic Fe-N<sub>2</sub> Mediator Promises Durable Li-S Batteries, *Adv. Mater.* 34 (2022) 2202256.
- [30] Z. Liang, J. Shen, X. Xu, F. Li, J. Liu, B. Yuan, Y. Yu, M. Zhu, Advances in the Development of Single-Atom Catalysts for High-Energy-Density Lithium-Sulfur Batteries, *Adv. Mater.* 34 (2022) 2200102.
- [31] F. Zhang, Z. Tang, L. Zheng, T. Zhang, M. Xu, H. Xiao, H. Zhuang, P. Han, Q. Gao, Edge-distributed iron single-atom moiety with efficient “trapping-conversion” for polysulfides driving high-performance of Li-S battery, *Appl. Catal. B Environ.* 334 (2023), 122876.
- [32] W. Zhang, Y. Chao, W. Zhang, J. Zhou, F. Lv, K. Wang, F. Lin, H. Luo, J. Li, M. Tong, E. Wang, S. Guo, Emerging Geminal-Atomic-Site Catalysts for Efficient Energy Catalysis, *Adv. Mater.* 33 (2021) 2102576.
- [33] L. Li, K. Yuan, Y. Chen, Breaking the scaling relationship limit: from single-atom to geminal-atom catalysts, *Acc. Mater. Res.* 3 (2022) 584–596.
- [34] M.-H. Xu, Y.-H. Wang, W.-H. He, X.-D. Li, X.-H. Meng, C.-C. Li, X.-T. Li, Q.-H. Kong, L. Shen, J. Zhang, X. Zhang, S. Xin, Y.-G. Guo, A. N-Rich, porous carbon nanocube anchored with Co/Fe geminal atoms: an efficient bifunctional catalytic host for Li-S batteries, *Mater. Chem. Front.* 6 (2022) 2095–2102.
- [35] L. Ma, J. Qian, Y. Li, Y. Cheng, S. Wang, Z. Wang, C. Peng, K. Wu, J. Xu, I. Manke, C. Yang, P. Adelhelm, R. Chen, Binary Metal Single Atom Electrocatalysts with Synergistic Catalytic Activity toward High-Rate and High Areal-Capacity Lithium-Sulfur Batteries, *Adv. Funct. Mater.* 32 (2022) 2208666.
- [36] X. Sun, Y. Qiu, B. Jiang, Z. Chen, C. Zhao, H. Zhou, L. Yang, L. Fan, Y. Zhang, N. Zhang, Isolated Fe-Co heteronuclear diatomic sites as efficient bifunctional catalysts for high-performance lithium-sulfur batteries, *Nat. Commun.* 14 (2023) 291.
- [37] T. Huang, Y. Sun, J. Wu, Z. Shi, Y. Ding, M. Wang, C. Su, Y. Li, J. Sun, , Altering Local Chemistry of Single-Atom Coordination Boosts Bidirectional Polysulfide Conversion of Li-S Batteries, *Adv. Funct. Mater.* 32 (2022) 2203902.
- [38] X. Zhou, J. Gao, Y. Hu, Z. Jin, K. Hu, K.M. Reddy, Q. Yuan, X. Lin, H.J. Qiu, Theoretically Revealed and Experimentally Demonstrated Synergistic Electronic Interaction of CoFe Geminal-Metal Sites on N-doped Carbon for Boosting Both Oxygen Reduction and Evolution Reactions, *Nano Lett.* 22 (2022) 3392–3399.
- [39] J. Jin, Z. Sun, T. Yan, Z. Shi, M. Wang, T. Huang, Y. Ding, J. Cai, P. Wang, L. Zhang, J. Sun, Demystifying activity origin of M–N–C single-atomic mediators toward expedited rate-determining step in Li–S electrochemistry, *Small Sci.* 2 (2022) 2200059.
- [40] C. Luo, X. Liang, Y. Sun, W. Lv, Y. Sun, Z. Lu, W. Hua, H. Yang, R. Wang, C. Yan, J. Li, Y. Wan, Q.-H. Yang, An organic nickel salt-based electrolyte additive boosts homogeneous catalysis for lithium-sulfur batteries, *Energy Storage Mater.* 33 (2020) 290–297.
- [41] G. Li, W. Lei, D. Luo, Y. Deng, Z. Deng, D. Wang, A. Yu, Z. Chen, Stringed “tube on cube” nanohybrids as compact cathode matrix for high-loading and lean-electrolyte lithium-sulfur batteries, *Energy Environ. Sci.* 11 (2018) 2372–2381.
- [42] W. Huang, Z. Lin, H. Liu, R. Na, J. Tian, Z. Shan, Enhanced polysulfide redox kinetics electro-catalyzed by cobalt phthalocyanine for advanced lithium-sulfur batteries, *J. Mater. Chem. A* 6 (2018) 17132–17141.
- [43] M. Wang, Z. Sun, H. Ci, Z. Shi, L. Shen, C. Wei, Y. Ding, X. Yang, J. Sun, Identifying the evolution of selenium-vacancy-modulated MoSe<sub>2</sub> precatalyst in lithium-sulfur Chemistry, *Angew. Chem. Int. Ed.* 60 (2021) 24558–24565.
- [44] Z. Zhao, Z. Yi, Y. Duan, R. Pathak, X. Cheng, Y. Wang, J.W. Elam, X. Wang, Regulating the d-p band center of FeP/Fe<sub>2</sub>P heterostructure host with built-in electric field enabled efficient bidirectional electrocatalyst toward advanced lithium-sulfur batteries, *Chem. Eng. J.* 463 (2023), 142397.
- [45] Z. Zhao, Y. Duan, F. Chen, Z. Tian, R. Pathak, J.W. Elam, Z. Yi, Y. Wang, X. Wang, Multifunctional transitional metal-based phosphide nanoparticles towards improved polysulfide confinement and redox kinetics for highly stable lithium-sulfur batteries, *Chem. Eng. J.* 450 (2022), 138310.
- [46] Z. Zhao, Z. Yi, H. Li, R. Pathak, Z. Yang, X. Wang, Q. Qiao, Synergetic effect of spatially separated dual co-catalyst for accelerating multiple conversion reaction in advanced lithium sulfur batteries, *Nano Energy* 81 (2021), 105621.